

Article

Comprehensive Investigation of the Durability of Lithium-Ion Batteries Under Frequency Regulation Conditions

Yuxin Tian ^{1,2,3}, Liye Wang ^{1,2,3,*}, Chenglin Liao ^{1,2,3} and Guifu Yan ^{1,2,3}

¹ Key Laboratory of Power Electronics and Electric Drives, Institute of Electrical Engineering, Chinese Academy of Sciences, Beijing 100190, China; tianyuxin@mail.iee.ac.cn (Y.T.); liaocl@mail.iee.ac.cn (C.L.); yangguifu@mail.iee.ac.cn (G.Y.)

² Institute of Electrical Engineering, Chinese Academy of Sciences, Beijing 100190, China

³ University of Chinese Academy of Sciences, Beijing 101408, China

* Correspondence: wangliye@mail.iee.ac.cn

Abstract: Due to the large-scale use of renewable energy generation and its lack of inertia, the frequency of the grid is extremely unstable. At the same time, with the vigorous development of new energy vehicles, large-scale power batteries have huge potential for renewable energy consumption. In this context, the Vehicle-to-Grid (V2G) method is proposed. Electric vehicles are used as energy storage systems to provide frequency regulation services as flexible power grid resources. However, when electric vehicles are invested in large-scale frequency regulation, their own power battery durability will also be affected. Based on this problem, the pseudo-two-dimensions (P2D) model of the battery was established in this paper, and the effects of temperature, state of charge (SOC), reported power, and frequency regulation conditions on battery capacity attenuation and negative potential distribution were explored through experiments and simulations.

Keywords: pseudo-two-dimensions (P2D) model; state of charge (SOC); negative potential distribution; battery durability



Academic Editors: Chris Mi, Zhi Cao and Naser Vosoughi Kurdkandi

Received: 18 January 2025

Revised: 9 February 2025

Accepted: 12 February 2025

Published: 14 February 2025

Citation: Tian, Y.; Wang, L.; Liao, C.; Yan, G. Comprehensive Investigation of the Durability of Lithium-Ion Batteries Under Frequency Regulation Conditions. *Batteries* **2025**, *11*, 75.

<https://doi.org/10.3390/batteries11020075>

Copyright: © 2025 by the authors. Licensee MDPI, Basel, Switzerland. This article is an open access article distributed under the terms and conditions of the Creative Commons Attribution (CC BY) license (<https://creativecommons.org/licenses/by/4.0/>).

1. Introduction

The large-scale investment in renewable energy makes the modern power system shift from the system based on rotary generators to the system based on inverters. Although this is very beneficial for the collection and utilization of renewable energy, because the power generation through the inverter does not provide enough mechanical inertia, it leads to insufficient inertia in the power system [1]. Because the moment of inertia has the ability to hinder the oscillation of the system and the frequency change speed is related to the moment of inertia, when the inertia of the system is insufficient, no matter what degree of power disturbance, it will lead to significant frequency fading and finally the frequency instability problem. At present, the main method to solve this problem is to add some virtual inertia into the system and deploy it appropriately to provide enough inertial response so as to enhance the stability of the system.

When the new energy power generation system is put into the industry on a large scale, considering the volatility characteristics of photovoltaic and wind power generation, the battery energy storage system will play a crucial role in the microgrid to maintain the continuous power supply for electric vehicle charging [2]. If the electric vehicle is charged without order in the power grid, it will cause the power grid load fluctuation to increase; that is, the peak value of the power grid fluctuation curve will increase. If the electric vehicle is charged orderly in the grid, that is, the V2G method, it will make the grid load

“cut peak and fill valley”. This method is widely used to adjust the frequency stability of the power grid, that is, through the power grid to regulate the charging and discharging power of electric vehicles, to provide auxiliary services for the power grid such as peak regulation, frequency regulation, and promotion of new energy consumption.

Although the power battery is beneficial to the stability of the power grid in the process of frequency modulation, its own life will also be affected to a certain extent. In the large-scale application of V2G technology, the study of battery durability is the core scientific issue of system design and economic evaluation. Because the V2G bidirectional charge and discharge mode can significantly change the operating boundary conditions of the battery, the asymmetric cycle condition caused by it will cause the electrochemical system to be subjected to multi-dimensional stress coupling. The reciprocating insertion/withdrawal of lithium ions between positive and negative electrodes will aggravate the lattice distortion of electrode materials and the dynamic reconstruction of the solid electrolyte interface (SEI) film. Meanwhile, frequent shallow charging and discharge cycles may lead to continuous loss of active lithium in the local state of charge (SOC) region, accelerating capacity decay. The random power fluctuation introduced by the grid dispatching demand will deteriorate the thermodynamic state of the battery, resulting in the accumulation of mechanical stress induced by temperature gradient. These multi-physics coupling degradation mechanisms will not only shorten the battery service life but also directly affect the energy handling capacity of the V2G system and the reliability of grid auxiliary services. Therefore, to establish a battery durability prediction model based on a cyclic attenuation mechanism, it is necessary to focus on quantifying the nonlinear relationship between capacity fade rate and internal resistance rise under dynamic working conditions. By constructing a state of health (SOH) prediction framework considering the synergistic effect of calendar aging and cycle aging, the life optimization design of the V2G charging and discharging strategy is realized. These will provide theoretical support for V2G’s participation in the power market for battery residual value assessment, energy storage capacity allocation optimization, and life-cycle carbon footprint calculation, and ultimately achieve the dual goals of sustainable utilization of battery assets and improvement of grid elasticity in V2G technology. At present, determining the aging and degradation mechanism of the battery is the most important and most challenging goal, and the interaction of multiple factors in the use environment or use mode makes the battery produce different aging effects; that is, the capacity loss and the increase in internal resistance do not depend on the same variables, so these processes are not single but complex. This makes understanding battery aging a difficult task [3]. Over the years, many studies have attempted to explore the effects of battery aging more deeply.

Li Y. et al. [4] took electric vehicles as reactive power compensation devices to participate in voltage regulation of the power grid. The research results show that with the increase in the number of electric vehicles connected to the grid, electric vehicles can assist or even replace traditional reactive power compensation devices and obtain better voltage control performance. In order to alleviate the huge impact of disorderly charging of large-scale electric vehicles on the distribution network. Considering that the reduction in battery life will directly affect the economic benefits and sustainability of the V2G system, the battery capacity protection research usually quantifies the battery aging generated during the V2G process by different means and introduces the objective function. There are also some studies that limit battery aging to an acceptable range by adding constraints. Li S. et al. [5] pointed out that traditional methods for quantifying battery aging, such as electrochemical models and artificial intelligence algorithms, can only quantify battery degradation on a large time scale. Ebrahimi M. et al. [6] considered both cycle aging and

calendar aging of batteries in the V2G process, but they believed that calendar aging only had a linear relationship with time.

Because lithium-ion batteries contain a variety of different chemical materials, the internal structure is very complex, and these materials will produce a variety of complex side reactions during the battery charging and discharging process, resulting in diversified aging mechanisms. Different aging modes will affect each other, and the same aging mechanism may lead to multiple aging modes. Battery temperature, SOC, charge/discharge ratio, depth of discharge, and cycle times are the main factors affecting battery aging [7]. Therefore, in order to study the durability of batteries, it is necessary to establish a perfect battery aging model. There are many kinds of battery aging models, and the accuracy, calculation amount, and application range of different models are different. At present, electrochemical models, empirical models, and semi-empirical models are commonly used in mainstream research. In the 1990s, Newman's group tried to estimate battery performance based on the Butler–Volmer equation and the theory of porous electrodes. Darling and Newman [8] for the first time tried to simulate the aging process in an electrochemical model and realized a simple solvent oxidation reaction, obtained good results, and gave a good conclusion on the selection of solvents. Dalverny et al. [9] determined the morphology of the LiCoO₂ electrode by ab initio calculation. In addition, the phase transition process of lithium iron phosphate (LFP) active particles was also theoretically studied. Ab initio calculations can explain battery aging by estimating the energy associated with solvent decomposition or dissolution of lithium components. Tasaki et al. [10] have linked the dissolution of lithium salts near the negative solid electrolyte interface (SEI) to calendar aging. As for empirical models, the aging model based on Arrhenius is the most widely used. Based on the empirical formula of the relationship between chemical reaction rate constant and temperature, the model can model cyclic aging and calendar aging, respectively, when various stress factors are comprehensively considered [7]. In recent years, with the development of artificial intelligence technology, the battery aging model based on a neural network can accurately reflect the relationship between various factors and capacity decay without establishing complicated mathematical expressions and updating network parameters through training [11]. The semi-empirical aging model not only has the simplicity and ease of use of the empirical model but also makes full use of the basic knowledge of the physical and chemical characteristics of the battery, which is very suitable for offline analysis. The Arrhenius formula is used to correct the growth of the SEI film and electrolyte loss during the initial use of the battery in the electrochemical model, which improved the accuracy of the model under different environments [12]. Based on the hypothesis that SEI film growth leads to battery degradation, Ecker M. et al. [13] combined the electrothermal model with empirical mathematical expressions to establish a semi-empirical aging model that can analyze battery degradation under different electrothermal environments. The lithium evolution behavior of lithium-ion batteries is one of the key factors leading to battery life decay, and the lithium evolution situation of batteries is mainly reflected by the negative electrode position of the battery, so this study will mainly focus on the analysis of the negative electrode potential distribution of lithium-ion batteries under the frequency modulation condition.

Through the above findings, the existing models, mostly based on laboratory-accelerated aging data, fail to effectively reflect the irregular charge–discharge characteristics brought by the grid demand response in the actual V2G working conditions. Secondly, the current economic analysis generally adopts a linear attenuation model, ignoring key nonlinear factors such as temperature change, charge and discharge rate, SOC, discharge depth heterogeneity, and calendar aging coupling effect. Third, most studies

focus on battery degradation but do not establish a dynamic optimization model between battery degradation and power grid frequency fluctuations.

The goal of this study is to minimize the attenuation of lithium-ion batteries and maximize the benefits of the grid while controlling the frequency stability of the grid. Firstly, the typical frequency regulation conditions are obtained in the American PJM market. Secondly, a P2D model related to lithium-ion batteries was built by studying the power performance and durability mechanism of lithium-ion batteries, and the above conditions were input into the model to investigate the distribution of the model's negative potential under different SOC, temperature, and reported power, and the results were analyzed to find out the influence of different factors on the battery. The research route is shown in Figure 1. In the future, the frequency regulation model will be built according to the relevant knowledge of the power system, and the P2D model will be built according to the above results, and the two will be coupled. The coupling model is optimized to minimize the negative impact on the negative battery potential. At the same time, it is also necessary to consider that electric vehicles participate in the frequency regulation of the grid, and the grid gains the most benefits.

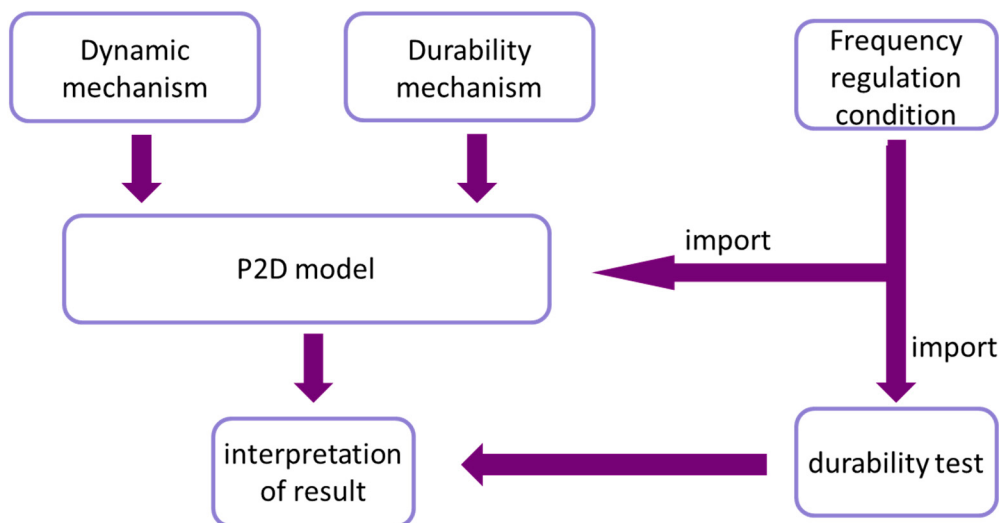


Figure 1. Research framework.

2. P2D Electrochemical Model Development

Based on the theory of porous electrodes, the battery P2D model describes the mass transfer, dynamics, thermodynamics, and other processes inside the battery through a set of partial differential equations. On the basis of the basic composition, the P2D model has the following three core assumptions: the electrode material is composed of spherical particles; the double-layer effect is not considered; and the positive and negative collector conductivities are very high, so the collector does not change significantly in the y - and z -axes; in other words, the electrochemical reaction dynamics only work in the x -axis. These three core assumptions simplify the battery model building process at three levels. The regular porous structure of spherical particles avoids the complex structure and particle distribution of active substances in practice, which is the most basic physical simplification method. Secondly, avoiding the double-layer effect can greatly simplify the distribution of ions on the electrolyte and electrode surface. Limiting the electrochemical dynamics to the x -axis further facilitates the mathematical processing. The internal structure of the battery is roughly shown in Figure 2. To study a battery from a mechanism point of view, it is necessary to investigate its internal material distribution and potential distribution, corresponding to the material transfer and charge transfer within the battery, respectively.

Therefore, in order to quantitatively describe the P2D model, it is necessary to establish the solid–liquid phase potential distribution, solid–liquid-phase diffusion process, electrochemical reaction model of interfacial reaction, and charge conservation as constraints. The following process is shown.

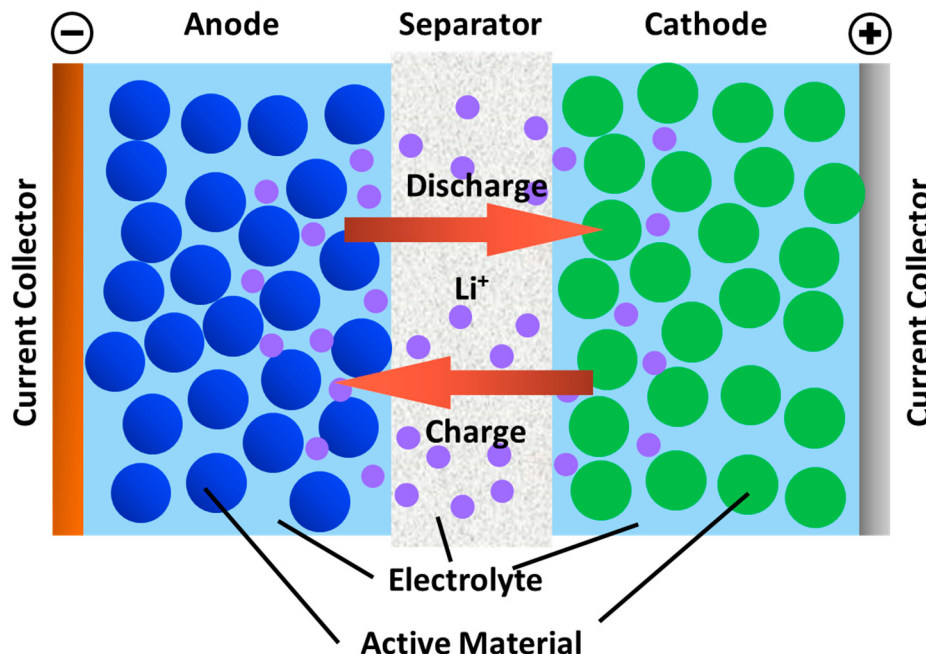


Figure 2. Battery internal structure diagram.

Solid-phase potential distribution: According to the conductivity of the electrode material, the relationship between current and potential gradient can be expressed (Equation (1)) as follows:

$$-\sigma_s^{eff} \frac{\partial \varphi_s}{\partial x} = i_s \quad (1)$$

where σ_s^{eff} is a solid-phase effective conductivity; φ_s is the potential for solid phase; and i_s is the current density. The minus sign in the formula is because the x direction takes the negative extreme as the origin during modeling, and the field strength and current direction are opposite; that is, the current inside the battery flows from the negative electrode to the positive electrode, while the field strength points from the positive electrode to the negative electrode. The boundary conditions for this equation are expressed as Equations (2) and (3).

$$\sigma_s^{eff} \frac{\partial \varphi_s}{\partial x} \Big|_{x=0} = -\sigma_s^{eff} \frac{\partial \varphi_s}{\partial x} \Big|_{x=L_{an}+L_{sep}+L_{ca}} = i_{app} \quad (2)$$

$$\frac{\partial \varphi_s}{\partial x} \Big|_{x=L_{an}} = \frac{\partial \varphi_s}{\partial x} \Big|_{x=L_{an}+L_{sep}} = 0 \quad (3)$$

Liquid-phase potential distribution: According to the liquid-phase conductivity and particle-specific surface area, the relationship between the potential gradient and lithium-ion concentration, reaction rate, temperature, and current can be expressed through Equation (4).

$$\frac{\partial}{\partial x} \left(\sigma_e^{eff} \frac{\partial \varphi_e}{\partial x} \right) = -aFj_n + \frac{2RT(1-t_+^0)}{F} \frac{\partial}{\partial x} \left(\sigma_e^{eff} \frac{\partial \ln c_e}{\partial x} \right) \quad (4)$$

where σ_e^{eff} is the liquid effective conductivity; φ_e is the potential for the liquid phase; j_n is the solid–liquid junction chemical reaction rate per unit area; a is the particle-specific surface area; F is the Faraday constant; t_+^0 is the lithium-ion transference number; R is the state of the ideal gas constant; T is the battery temperature; and c_e is the liquid lithium-ion concentration. Integrating x on both sides of this equation yields the following equation (Equation (6)), where the boundary condition is shown.

$$\sigma_e^{eff} \frac{\partial \varphi_e}{\partial x} = -i_s + \frac{2RT(1-t_+^0)}{F} \sigma_e^{eff} \frac{\partial \ln c_e}{\partial x} \quad (5)$$

$$\left. \frac{\partial \varphi_e}{\partial x} \right|_{x=0} = \left. \frac{\partial \varphi_e}{\partial x} \right|_{x=L_{an}+L_{sep}+L_{ca}} = 0 \quad (6)$$

Solid-phase ion diffusion: According to the solid-phase diffusion coefficient, the distribution of lithium-ion concentration over time in the polar diameter direction can be obtained via the following equation:

$$\frac{\partial c_s}{\partial t} = \frac{1}{r^2} \frac{\partial}{\partial r} \left(D_s r^2 \frac{\partial c_s}{\partial r} \right) \quad (7)$$

where c_s is the solid lithium-ion concentration; D_s is the solid-phase diffusion coefficient; t is time; and r is the pole size. This equation is a polar form of Fick's second law and represents the diffusion process of matter driven only by concentration. In the P2D model, the lithium ions of the porous electrode are removed or generated from the surface of active particles, so the lithium ions inside active particles will appear as a concentration gradient and will only be driven by it; therefore, the diffusion process of lithium ions in the solid particles can be described by this model. The boundary conditions are shown as Equations (8) and (9).

$$\left. -D_s \frac{\partial c_s}{\partial r} \right|_{r=0} = 0 \quad (8)$$

$$\left. -D_s \frac{\partial c_s}{\partial r} \right|_{r=R_s} = j_n \quad (9)$$

where R_s is the grain boundary radius, and j_n is the molar flow rate for ions.

Liquid-phase ion diffusion: Based on the diffusion coefficient and porosity of the liquid phase, and combined with the reaction process, the distribution of lithium-ion concentration in the liquid phase with time can be obtained via the following expression:

$$\varepsilon_e \frac{\partial c_e}{\partial t} = \frac{\partial}{\partial x} \left(D_e^{eff} \frac{\partial c_e}{\partial x} \right) + (1-t_+^0) a j_n \quad (10)$$

where c_e is the liquid lithium-ion concentration; D_e^{eff} is the liquid-phase diffusion coefficient; ε_e is the electrode porosity; t is time; t_+^0 is the lithium-ion transference number; j_n is the solid–liquid junction chemical reaction rate per unit area; and a is the particle-specific surface area. This is a revision of Fick's second law, where lithium ions migrate from the negative active particles into the electrolyte diffusion, and eventually become embedded in the positive active particles. There is a lithium-ion concentration gradient in the battery internal electrolyte; this concentration gradient is driven by lithium-ion diffusion, and, at the same time, by the internal electric field and migration. The boundary conditions are shown in Equation (11).

$$\left. \frac{\partial c_e}{\partial t} \right|_{x=0} = \left. \frac{\partial c_e}{\partial t} \right|_{x=L_{an}+L_{sep}+L_{ca}} = 0 \quad (11)$$

Solid-charge conservation: As a constraint to the P2D model, it describes that the number of disembedded or generated lithium ions during the reaction is equal to the number of charge transfer, as shown in Equation (12).

$$-\frac{\partial i_s}{\partial x} = \sigma_s^{eff} \frac{\partial^2 \varphi_s}{\partial x^2} = aFj_n \quad (12)$$

where j_n is the solid–liquid junction chemical reaction rate per unit area; a is the particle-specific surface area; F is the Faraday constant; σ_s^{eff} is the solid-phase effective conductivity; φ_s is the potential for solid phase; and i_s is the current density. Boundary conditions are expressed via Equation (13).

$$\left. \frac{\partial \varphi_s}{\partial x} \right|_{x=L_{an}} = \left. \frac{\partial \varphi_s}{\partial x} \right|_{x=L_{an}+L_{sep}} = 0 \quad (13)$$

Solid–liquid interface reaction: According to the Butler–Volmer equation of the electrochemical reaction of lithium ions during deintercalation and formation at the solid–liquid interface, changes in the current of the electrode and changes in the electrode potential can be described through Equation (14).

$$j_n = i_0 \left[\exp\left(\frac{\alpha_{an}F}{RT} \eta_{act}\right) - \exp\left(-\frac{\alpha_{ca}F}{RT} \eta_{act}\right) \right] \quad (14)$$

where j_n is the current density; i_0 is the exchange-current density; α_{an} and α_{ca} are migration coefficients of anions and cations, respectively; η_{act} is the electrode potential; R is the state of the ideal gas constant; and T is the battery temperature.

After the mathematical foundation of the P2D model is completed, parameter identification of the research object is needed to further calibrate the parameters required by the P2D model. Finally, a model was built in the COMSOL Multiphysics® ver5.6 simulation software. The model is shown in Figure 3. To achieve subsequent measurements, 20 probes were selected at an interval of 1×10^{-5} m and numbered 120 from left to right.

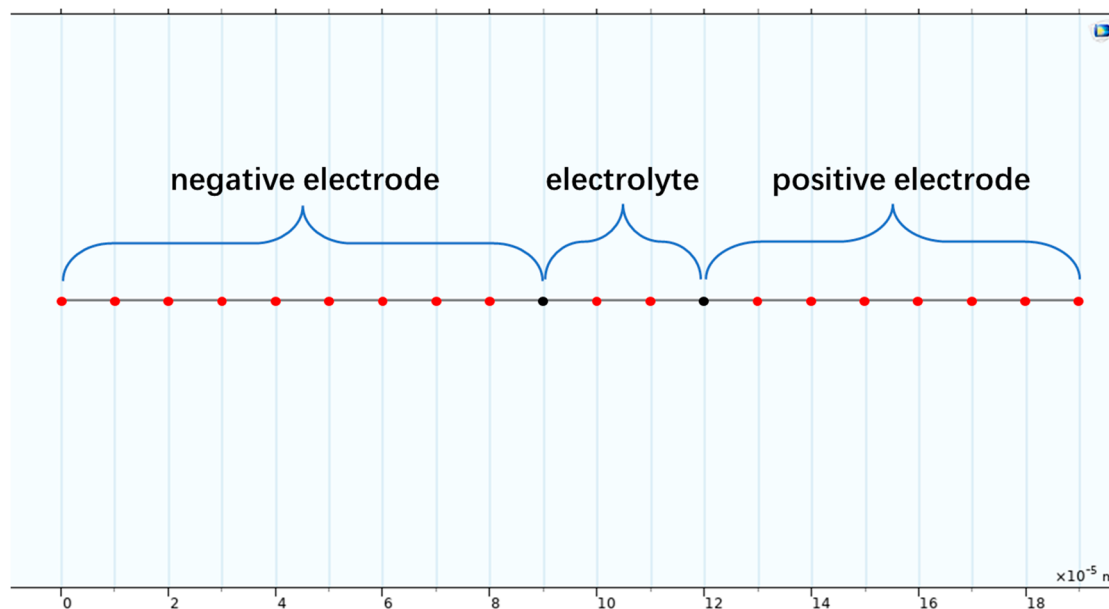


Figure 3. P2D model in COMSOL.

3. Experimental Setup

3.1. Durability Test Design

In this study, a 51 Ah ternary aluminum shell power lithium battery is used, and its nominal voltage is 3.7 V. The battery is suitable for a charging operating temperature of 20 °C to 50 °C, a discharge operating temperature from –20 °C to 50 °C, a charging limit voltage of 4.2 V, a discharge cut-off voltage of 2.7 V, and a main size of 148 × 27 × 92 mm.

In the battery durability test, the calendar aging of the battery is often ignored, and only cyclic aging is considered; that is, the battery is continuously charged and discharged, and the loss of battery capacity is investigated when a certain number of cycles are reached. In this study, the durability of the battery is explored under the frequency modulation condition, which can be regarded as the superposition of different pulse conditions, as shown in Figure 4. The following four test variables were selected for this test: SOC, half-pulse period, power, and temperature. The corresponding relationship between specific variables and levels is shown in Table 1.

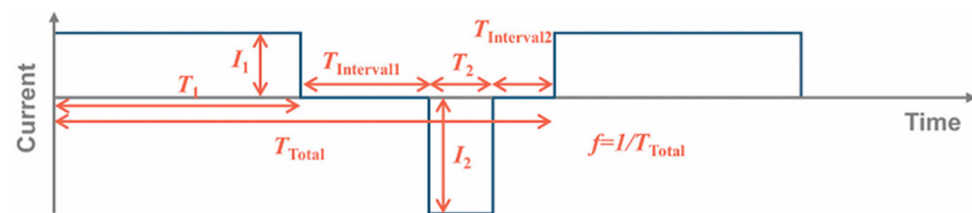


Figure 4. The superposition of different pulse conditions.

Table 1. Durability test variables.

Level	Factor 1	Factor 2	Factor 3	Factor 4
	SOC	Half-Pulse Period (s)	Power	Temperature (°C)
1	0.2	2	0.1 C*V	0
2	0.5	150	0.5 C*V	25
3	0.8	300	1 C*V	45

According to the factors and levels given in this table, a total of 81 sets of tests are required, covering all factor combinations. However, the durability test is a time-consuming test with limited equipment. In order to solve the problem of excessive number of tests and to cover the influence of various factors on the test results, the orthogonal test method was adopted in this study to simplify the number of experimental groups. This method has the characteristics of uniform dispersion and neat comparability. The final orthogonal test factor combination is shown in Table 2, with a total of 9 groups of tests. In this study, 9 batteries were tested and numbered, the same as the orthogonal test numbers; each cell corresponds to a set of factor combinations, and its capacity attenuation was measured after several cycles.

Each durability test consists of approximately 18 h of capacity testing and 50 h of bidirectional pulse tests. The capacity test mainly includes the following processes: the battery is placed in a 25 °C incubator to fully charge; constant discharge is set at 17 A to 2.5 V, let stand; charge is set at 17 A; constant current is set to 4.2 V to fully charge and stand; and repeat the process 3 to 5 times. The current capacity of lithium-ion battery can be obtained by calculating the average of multiple discharge capacities by the ampere-hour integration method. After the battery capacity is measured, the battery is tested in a bidirectional pulse condition according to the combination of test factors; each test lasts about 50 h, and the capacity test is carried out after each bidirectional pulse

condition test, i.e., a durability test. Three rounds of durability tests were carried out in this study.

Table 2. Durability test orthogonal table.

No.	Factor 1	Factor 2	Factor 3	Factor 4
1	1	1	1	1
2	1	2	3	2
3	1	3	2	3
4	2	1	3	3
5	2	2	2	1
6	2	3	1	2
7	3	1	2	2
8	3	2	1	3
9	3	3	3	1

3.2. Negative Potential Simulation Test Design

In order to explore the influence of multiple factors on the negative battery potential, the following four factors were selected: SOC, temperature, reported power, and frequency regulation condition. Each factor is selected according to its characteristics that meet the actual needs of several levels. Reported power refers to the maximum capacity of the battery allowed to participate in frequency regulation, calculated by the product of the maximum current and the average voltage. The average voltage refers to the highest cut-off voltage and the lowest cut-off voltage, so the reported power can also reflect the full rate value of the battery participating in frequency modulation charge and discharge current.

As for frequency regulation condition, based on the PJM history instruction frequency regulation 2020, selected has the following characteristics of six kinds of typical working conditions: (1) the maximum frequency of full-rate charge and discharge; (2) the minimum frequency of full-rate charge and discharge; (3) the maximum frequency regulation mileage; (4) the minimum frequency regulation range; (5) the maximum integral value of current with respect to time in charge and discharge process; and (6) the minimum integral value of current with respect to time in charge and discharge process. The corresponding relationship between specific factors and levels is shown in Table 3. Six points of the frequency regulation condition correspond to levels 1 to 6 of factor 4, as seen in Table 3.

Table 3. Simulation test variables.

Level	Factor 1	Factor 2	Factor 3	Factor 4
	SOC	Temperature (°C)	Power	Frequency Regulation Condition
1	0.2	−10	0.1 C*V	p_1_max
2	0.4	0	0.5 C*V	p_1_min
3	0.6	25	1 C*V	m_max
4	0.8	45	2 C*V	m_min
5			3 C*V	int_max
6				int_min

Among them, frequency regulation mileage refers to the absolute value of the difference between the output value at the end of each control command and the output value of the command response after it is issued. In this study, it is the absolute value of the difference between adjacent two-second frequency regulation instructions, and the total frequency regulation mileage is the sum of frequency regulation mileage in the selected time interval. In order to make the selected frequency regulation conditions more universal and consider the complexity of the selection process, this study first selected four typical days in the whole year—March 1, June 1, September 1, and December 1—that is, one day

in each of the four seasons. Then, in these four days, with one minute as the step length, Matlab was used to calculate the full rate charge and discharge frequency. Frequency regulation mileage and the integral value of the current with respect to time in the charge and discharge process every 5 min were compared in order to obtain six five-minute frequency regulation conditions.

The same as the durability test, this part adopts the orthogonal test method and obtains 49 groups of simulation tests according to the above factor levels. The specific factor colocation is shown in Table 4.

Table 4. Simulation test orthogonal table.

No.	Factor 1	Factor 2	Factor 3	Factor 4
1	1	1	1	1
2	1	2	3	4
3	1	3	5	6
4	1	4	5	3
5	1	4	2	6
6	1	4	4	2
7	1	4	5	5
8	2	1	5	5
9	2	2	2	2
10	2	3	4	5
11	2	4	5	1
12	2	4	1	4
13	2	4	3	6
14	2	4	5	3
15	3	1	5	4
16	3	2	1	6
17	3	3	3	3
18	3	4	5	6
19	3	4	5	2
20	3	4	2	5
21	3	4	4	1
22	4	1	3	5
23	4	2	5	5
24	4	3	2	1
25	4	4	4	4
26	4	4	5	6
27	4	4	1	3
28	4	4	3	6
29	4	1	2	6
30	4	2	1	3
31	4	3	1	6
32	4	4	3	2
33	4	3	4	5
34	4	2	3	2
35	3	1	2	4
36	3	1	3	5
37	3	2	3	1
38	3	3	5	4
39	3	4	2	6
40	2	3	4	3
41	2	2	5	5
42	2	1	1	2
43	2	1	2	3
44	2	2	4	6
45	1	3	5	1
46	1	4	1	5
47	1	3	3	1
48	1	2	5	4
49	1	1	4	5

4. Result and Discussion

4.1. Durability Test Result

The capacity loss data obtained from the three-round durability test were recorded, respectively, and the corresponding data of the combination of test factors and capacity loss for each group were obtained, as shown in Table 5. Next, the range analysis method is used to analyze the capacity loss results. The range analysis has the advantages of simplicity and intuition and is suitable for screening results with low accuracy requirements. However, it cannot estimate the size of the error or accurately estimate the importance of the influence of various factors on the results. The results of three rounds of durability analysis are shown in Figure 5. The K_{avg} in this figure is the average value of the test data applied to a certain level of a factor. In order to obtain the comparison among levels within each factor, we can compare the impact of each level on capacity loss by comparing the K_{avg} of each level.

Table 5. Durability orthogonal test results.

No.	Factor 1	Factor 2	Factor 3	Factor 4	Capacity Loss (Ah)		
					The First Round	The Second Round	The Third Round
1	1	1	1	1	0.002646	0.03314	0.201544
2	1	2	3	2	0.00789	0.029742	0.126122
3	1	3	2	3	0.35454	0.38947	0.601268
4	2	1	3	3	0.405462	0.446374	0.66037
5	2	2	2	1	0.233194	0.192172	0.23746
6	2	3	1	2	0.031688	0.008698	0.145326
7	3	1	2	2	0.112026	0.182386	0.210076
8	3	2	1	3	0.12343	0.22568	0.289484
9	3	3	3	1	0.852186	1.10946	0.882492

Compared with factor 1, it can be seen that the impact of each round of SOC on capacity loss presents a positive correlation trend; that is, the capacity loss increases with the increase in SOC, and the capacity loss is the smallest when SOC is 0.2. This is because the battery SOC and the battery voltage are highly correlated, and the battery voltage can be derived when the battery SOC and current are known. For the battery, the higher the SOC, the higher the terminal voltage; that is, the lower the negative potential, which increases the rate of negative side reactions and SEI film thickening, the faster the battery aging rate and capacity loss.

The decrease in the pulse period indicates that the frequency of charge and discharge conversion is increasing; that is, the direction of movement of lithium ions in the electrolyte is constantly changing and the change rate is accelerating, which will lead to the acceleration of the diffusion rate of lithium ions in the electrolyte. Moreover, this is conducive to solving the lithium deposition structure, but not conducive to the occurrence of the lithium evolution reaction, ultimately resulting in reduced capacity loss. When the pulse period is too small, i.e., the frequency is too high, the internal reaction rate becomes too fast, resulting in a rise in battery temperature, which is not conducive to reducing capacity loss. This can be explained by the fact that factor 2 has the smallest capacity loss when the half-pulse period is 150 s.

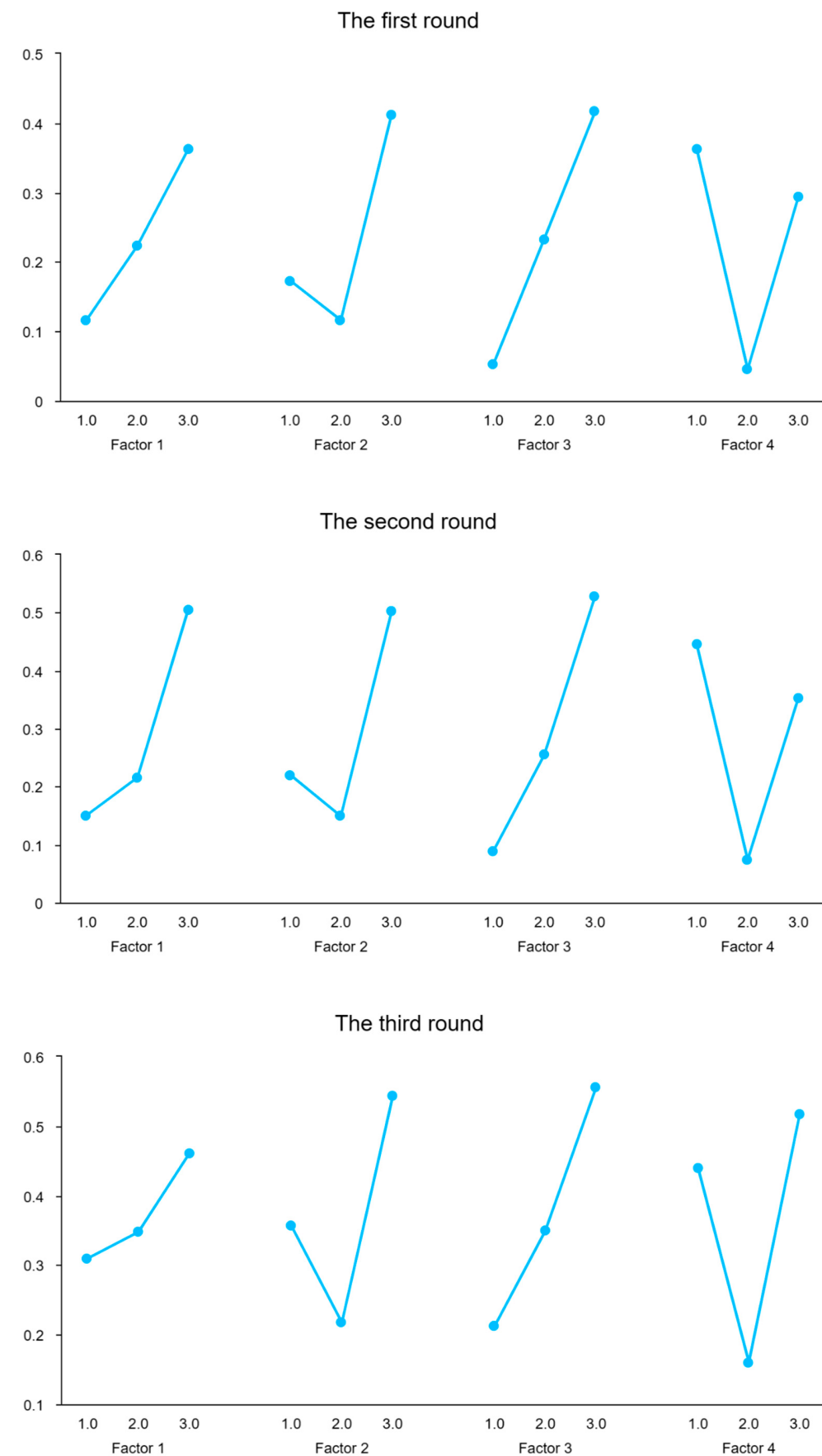


Figure 5. The K_{avg} of each level of the factor within first, second, and third rounds.

The reported power is related to the maximum charge and discharge currents—the greater the reported power, the greater the maximum charge and discharge current and the current during the charge and discharge process. Although this will accelerate the main reaction rate, it will also lead to the acceleration of the side reaction rate, which is conducive to the occurrence of lithium evolution reaction and SEI film thickening, making the loss of available lithium result in an increased capacity loss (factor 3 at 0.1 C*V) and minimum loss of battery capacity.

Compared with factor 4, it can be seen that each round of temperature has the smallest impact on capacity loss at 25 °C; that is, low and high temperatures bring greater capacity loss, which is in line with the appropriate operating temperature of general commercial batteries, i.e., 10–35 °C. This is because the temperature will affect the internal reaction rate of the battery. A temperature that is too high will speed up the reaction rate and the side reaction rate, resulting in an increased capacity loss. A temperature that is too low will lead to an increase in internal resistance, resulting in an intensified polarization phenomenon, which will lead to additional side reactions, especially at low temperatures. Charging may lead to the occurrence of lithium evolution, where the available lithium content is reduced so that the battery is rapidly degraded; the brittleness of the material at low temperatures will also affect battery life.

4.2. Negative Potential Simulation Test Results

The negative electrode potential refers to the solid–liquid-phase potential difference on the surface of the negative particle. When it is greater than the equilibrium potential of the lithium evolution reaction, the lithium evolution phenomenon will occur in the negative electrode of the battery. The phenomenon of lithium evolution leads to the appearance of lithium dendrites on the negative electrode surface, further leading to the loss of available lithium, increased polarization, and thus reduced battery capacity. Moreover, the longitudinal existence of a lithium-ion concentration gradient causes an uneven distribution of lithium dendrites, which will even puncture the diaphragm, resulting in a short circuit inside the battery. Therefore, the lithium evolution criterion can be expressed by Equation (15).

$$\varphi_s - \varphi_l < U_{e,2} \quad (15)$$

where φ_s is the solid-phase potential; φ_l is the liquid-phase potential; and $U_{e,2}$ is the lithium reaction equilibrium potential, usually considered to be 0 V (relative to Li/Li^+).

In this paper, the 15th group of test results is selected for display, as shown in Figure 6. Here, the abscissa of the thickness of the battery is present, the units are meters, and the diagram is the negative part of the selection, so the range is $[0.9 \times 10^{-5}]$ m. The ordinate is simulation time and the units are seconds, with a total of 300 s. The color diagram shows the negative electrode potential at the corresponding position and time, and the units are mV. To facilitate the detection of negative electrode potential, the color diagram interval is adjusted to $[-100, 50]$ mV.

It can be seen from the above-mentioned negative potential distribution results that some simulation groups have negative electrode potentials during the simulation process. Through the factor colocation of these groups, a qualitative conclusion can be obtained—under different working conditions, high SOC, low temperature, and high charging rate, negative electrode potential will appear negative. In addition, it can also be found that along the positive direction of the x -axis, the negative electrode potential has a decreasing trend; that is, the closer the electrode and the electrolyte interface, the smaller the negative electrode potential. Therefore, it is not only necessary to consider the influence of the time dimension on the negative potential, but also to take the x -axis direction into account. In order to better obtain the degree of influence of various factors

on this phenomenon, statistical means are used for quantitative analysis. Therefore, in this study, the part of the negative electrode potential is a double integral for time and the x -axis direction, which can be briefly written as $\varphi_{neg} \times t \times l$. The obtained integral value was analyzed. The specific results are shown in Table 6. In order to express the results easily, the simulation groups without negative electrode potentials are not included in Table 6; that is, the integral value of these groups is 0. Although these groups do not appear in Table 6, they must be included in the data analysis process.

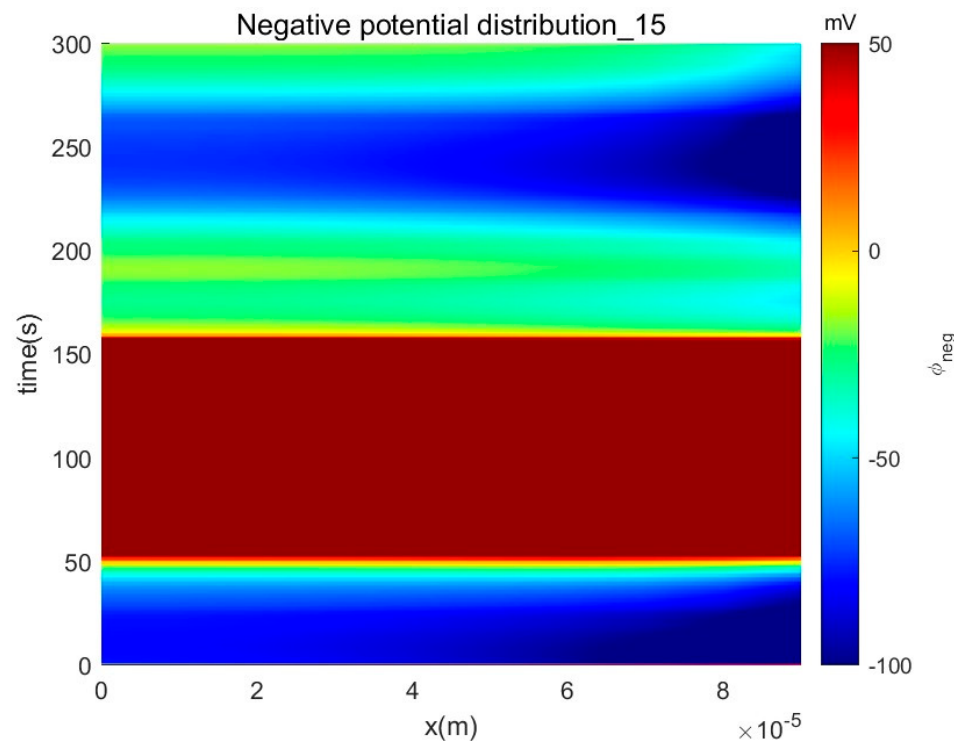


Figure 6. Negative potential distribution results.

Table 6. Negative potential negative integral result.

No.	Factor 1	Factor 2	Factor 3	Factor 4	$\varphi_{neg} \times t \times l$
2	1	2	3	4	0.00067558
8	2	1	5	5	0.4674
15	3	1	5	4	0.9619
22	4	1	3	5	0.3432
23	4	2	5	5	0.3573
35	3	1	2	4	0.1467
36	3	1	3	5	0.2518
37	3	2	3	1	0.8525
41	2	2	5	5	0.1939
43	2	1	2	3	0.7514
48	1	2	5	4	0.2517
49	1	1	4	5	0.1856

Multiple linear regression analysis among factor 1, factor 2, factor 3 and factor 4 were used as independent variables and dependent variables for multiple linear regression analyses. The R-square value of the model was 0.355, meaning that factor 1, factor 2, factor 3, and factor 4 could explain 35.5% of the variation of $\varphi_{neg} \times t \times l$. During the F-test of the model, it was found that the model passed the F-test ($F = 6.049$, $p = 0.001 < 0.05$), indicating that at least one of the factors (factor 1, factor 2, factor 3, and factor 4) would have an impact on $\varphi_{neg} \times t \times l$. In addition, by testing the multicollinearity of the model,

it is found that the variance inflation factor (VIF) values in the model are all less than 5, which means that there is no collinearity problem, and the D-W value is near the number 2, which indicates that there is no autocorrelation in the model and there is no correlation between the sample data. The final analysis results showed that the regression coefficients corresponding to factor 1, factor 2, factor 3, and factor 4 were 0.021 ($t = 0.852, p = 0.399 > 0.05$), -0.110 ($t = -4.687, p = 0.000 < 0.01$), 0.040 ($t = 2.098, p = 0.042 < 0.05$), and -0.008 ($t = -0.512, p = 0.611 > 0.05$), respectively.

It means that factor 2 has a significant negative correlation with $\varphi_{neg} \times t \times l$; that is, it has the greatest impact on the result at $-10\text{ }^{\circ}\text{C}$. Factor 3 has a significant positive correlation with $\varphi_{neg} \times t \times l$; that is, it has the greatest impact on the result when the maximum charging rate is 3 C. Factor 1 and factor 4 have no significant correlation with $\varphi_{neg} \times t \times l$.

Multiple linear regression analysis in factors: In order to further analyze the internal influences of factor 1 and factor 4 on $\varphi_{neg} \times t \times l$, internal multiple linear regression analysis was used, respectively. Firstly, factor 1 is analyzed, and level 1 is taken as a reference, and the linear regression coefficients of the four levels are 0.036, 0.081, 0.148, and 0.017, respectively. Compared with the linear regression coefficients of the other three levels, it can be seen that the coefficient at level 3 is the largest, so it can be considered that the SOC of 0.6 in factor 1 has the greatest impact on $\varphi_{neg} \times t \times l$. Next, factor 4 is analyzed, and level 1 is taken as a reference. The linear regression coefficients of the six levels are 0.122, -0.122 , 0.073, -0.014 , -0.122 , and 0.04. Comparing the linear regression coefficients of the other five levels, it can be seen that between level 1 and level 2, level 1 is larger; between level 3 and level 4, level 3 is larger; and between level 5 and level 6, level 6 is larger. Therefore, it can be considered that in factor 4, the maximum integral value of current with respect to time in the charge and discharge process, the maximum frequency of the full rate charge and discharge, and the minimum frequency regulation range have the greatest influence on $\varphi_{neg} \times t \times l$.

To summarize, the analysis of temperature and reported power aligns with expectations, indicating that a lower temperature and higher charging rate have a greater impact on negative potential below 0. However, regarding SOC, this study reveals that the greatest influence is not observed at SOC of 0.8. This discrepancy may be attributed to the fact that the orthogonal simulation test conducted in this study did not encompass all possible factor combinations, resulting in some results being influenced by factor coupling and thereby affecting the isolated effect of individual factors. Furthermore, improvements can be made to the test methodology by selecting frequency regulation conditions for quantitative evaluation across six levels before analyzing the joint influence of three other factors on the target under investigation.

4.3. Theoretical Analysis

For temperature, there are two main mechanisms to affect the electrochemical system of the battery, i.e., one is the Arrhenius Equation (16) and the other is the Stokes–Einstein Equation (17).

$$k = A \cdot e^{-\frac{E_a}{(RT)}} \quad (16)$$

$$D = \frac{k_B T}{6\pi\eta r} \quad (17)$$

where A refers to the pre-factor; E_a is the activation energy; R is the gas constant; T is the absolute temperature; D represents the diffusion coefficient of the molecule; k_B is the Boltzmann constant; η is the viscosity of the solvent; and r is the radius of the molecule. It can be seen that the increase in electrolyte viscosity at low temperature reduces the diffusion coefficient of lithium ions, leading to the increase in charge transfer impedance and ohmic

polarization. Furthermore, the kinetics of lithium embedding into negative graphite are hindered, and the concentration gradient of lithium ions on the negative surface increases, which may reduce the local potential to the lithium metal precipitation potential, form lithium dendrites, consume active lithium, and accelerate the SEI film rupture. At high temperatures, the side reaction accelerates, the dissolution or regeneration of the SEI film intensifies, the active lithium becomes continuously consumed, and the positive transition metal dissolves and migrates to the negative electrode to destroy the SEI film. Therefore, at low temperatures, the negative polarization increases, the potential distribution becomes more uneven, and the lithium threshold becomes easily reachable in local areas. At high temperatures, the SEI impedance decreases, the potential distribution becomes uniform, and the overall lithium loss accelerates. However, whether it is a high or low temperature, it will lead to a reduction in the effective lithium inventory, while the active material loss.

State of charge (SOC) directly affects the negative equilibrium potential, according to the Nernst Equation (18).

$$\varphi_{eq} = \varphi_0 + \frac{RT}{F} \ln \left(\frac{c_{Li^+}^{surf}}{c_{Li}^{max} - c_{Li^+}^{surf}} \right) \quad (18)$$

At high SOC, $c_{Li^+}^{surf}$ approaches c_{Li}^{max} , causing φ_{eq} to approach the lithium metal deposition threshold. At this time, the local current density distribution presents significant non-uniformity. The Butler–Volmer Equation (19) is expressed as follows:

$$j = j_0 \left[e^{\alpha_a F \eta / RT} - e^{\alpha_c F \eta / RT} \right] \quad (19)$$

When $\eta > 0$ (charging process), the high SOC region preferentially triggers the lithium evolution side reaction, resulting in irreversible capacity loss.

As for charge and discharge ratio, high ratio will cause third-order polarization coupling. One is the ohmic polarization, i.e., $\Delta\varphi_\Omega = I \cdot R_\Omega$, which is related to collector and electrolyte conductivity. The second is the electrochemical polarization, controlled by the Butler–Volmer kinetics. The third is the concentration polarization, which follows Fick's second law. The porous electrode theory shows that the local current density distribution satisfies Equation (20).

$$\nabla \cdot (\sigma_{eff} \nabla \phi_s) = a_s j \quad (20)$$

It can be seen that a significant concentration gradient is formed inside the pore of the electrode at a high power rate, leading to lithium deposition, preferentially in the edge region.

In addition, the half-pulse period affects the dynamic response characteristics of the electrode, and the characteristic time constant τ_{diff} is determined by the diffusion process Equation (21).

$$\tau_{diff} = \frac{L^2}{D} \quad (21)$$

where L is the diffusion characteristic length. When $\tau < \tau_{diff}$, the pulse process causes an unsteady-state concentration fluctuation, ultimately resulting in an “insufficient relaxation” effect. When $\tau > \tau_{diff}$, lithium ions can be fully redistributed. The high-frequency pulse leads to periodic potential oscillation on the surface of the negative electrode, which aggravates the mechanical stress damage of the SEI film.

5. Conclusions

In this paper, a large number of research studies on power grid frequency regulation, virtual inertia, and battery durability are investigated. The virtual inertia system and battery

life estimation models are introduced, and the advantages and disadvantages of each model are given. Based on the above-mentioned problems, the effects of temperature, SOC, half-pulse period, and reported power on battery capacity loss were investigated experimentally. The range analysis method is used to compare the difference in the influence of four factors on capacity loss; the internal influence of each factor is compared. In addition, in order to simplify the number of experimental groups, the orthogonal test method was also introduced.

Since the lithium evolution phenomenon of the battery will lead to the capacity loss of the battery, and the criterion that directly leads to the lithium evolution phenomenon states that the negative potential is less than zero, this study explored the influence of temperature, SOC, reported power, and frequency regulation conditions on the negative potential distribution of the battery and the degree of lithium evolution from the perspective of simulation. The P2D model was built according to the dynamic and durability mechanisms of lithium-ion batteries. The orthogonal test was also used to simplify the number of simulation groups; the negative electrode potential distribution diagram under each group of simulations and the qualitative results were obtained. Then, the battery thickness and simulation time are integrated with the negative electrode potential, and the integral value obtained is analyzed to obtain certain quantitative results.

Author Contributions: Conceptualization, Y.T. and L.W.; methodology, Y.T.; software, Y.T.; validation, Y.T.; formal analysis, Y.T.; investigation, Y.T.; resources, L.W.; data curation, L.W.; writing—original draft preparation, Y.T.; writing—review and editing, G.Y.; visualization, Y.T.; supervision, C.L.; project administration, L.W.; funding acquisition, L.W. All authors have read and agreed to the published version of the manuscript.

Funding: This research is supported by supported by the National Key Research and Development Program of China (Grant No.2023YFB2504100), the National Natural Science Foundation of China (52277228), the National Natural Science Foundation of China (52077208), and the Beijing Natural Science Foundation (L243021).

Data Availability Statement: The original contributions presented in this study are included within this article. Further inquiries can be directed to the corresponding author.

Conflicts of Interest: The authors declare no conflicts of interest. The funders had no role in the design of this study, in the collection, analysis, or interpretation of data, in the writing of the manuscript, or in the decision to publish the results.

Abbreviations

The following abbreviations are used in this manuscript:

SOC	state of charge
P2D	pseudo-two-dimensions
V2G	Vehicle-to-Grid
LFP	lithium iron phosphate
SEI	solid electrolyte interface

References

1. Caulfield, B.; Furszyfer, D.; Stefaniec, A.; Foley, A. Measuring the equity impacts of government subsidies for electric vehicles. *Energy* **2022**, *248*, 123588. [[CrossRef](#)]
2. Zou, W.; Li, J.; Yang, Q.; Wan, X.; He, Y.; Lan, H. A real-time energy management approach with fuel cell and battery competition-synergy control for the fuel cell vehicle. *Appl. Energy* **2023**, *334*, 120667. [[CrossRef](#)]
3. Capacity Degradation Minimization Oriented Optimization for the Pulse Preheating of Lithium-Ion Batteries Under Low Temperature—ScienceDirect. Available online: <https://www.sciencedirect.com/science/article/abs/pii/S2352152X20315838> (accessed on 18 January 2025).

4. Li, Y.; Li, L.; Peng, C.; Zou, J. An MPC based optimized control approach for EV-based voltage regulation in distribution grid. *Electr. Power Syst. Res.* **2019**, *172*, 152–160. [[CrossRef](#)]
5. Optimization of Bi-Directional V2G Behavior with Active Battery Anti-Aging Scheduling. Available online: <https://ieeexplore.ieee.org/document/8951120> (accessed on 18 January 2025).
6. Ebrahimi, M.; Rastegar, M.; Mohammadi, M.; Palomino, A.; Parvania, M. Stochastic Charging Optimization of V2G-Capable PEVs: A Comprehensive Model for Battery Aging and Customer Service Quality. *IEEE Trans. Transp. Electrif.* **2020**, *6*, 1026–1034. [[CrossRef](#)]
7. Vermeer, W.; Chandra Mouli, G.R.; Bauer, P. A Comprehensive Review on the Characteristics and Modeling of Lithium-Ion Battery Aging. *IEEE Trans. Transp. Electrif.* **2022**, *8*, 2205–2232. [[CrossRef](#)]
8. Darling, R.; Newman, J. Modeling Side Reactions in Composite LiyMn₂O₄ Electrodes. *J. Electrochem. Soc.* **1998**, *145*, 990. [[CrossRef](#)]
9. Dalverny, A.-L.; Filhol, J.-S.; Doublet, M.-L. Interface electrochemistry in conversion materials for Li-ion batteries. *J. Mater. Chem.* **2011**, *21*, 10134–10142. [[CrossRef](#)]
10. Tasaki, K.; Harris, S.J. Computational Study on the Solubility of Lithium Salts Formed on Lithium Ion Battery Negative Electrode in Organic Solvents. *J. Phys. Chem. C* **2010**, *114*, 8076–8083. [[CrossRef](#)]
11. Chaoui, H.; Ibe-Ekeocha, C.C. State of Charge and State of Health Estimation for Lithium Batteries Using Recurrent Neural Networks. *IEEE Trans. Veh. Technol.* **2017**, *66*, 8773–8783. [[CrossRef](#)]
12. Degradation Cost Analysis of Li-Ion Batteries in the Capacity Market with Different Degradation Models. Available online: <https://www.mdpi.com/2079-9292/9/1/90> (accessed on 18 January 2025).
13. Ecker, M.; Gerschler, J.B.; Vogel, J.; Käbitz, S.; Hust, F.; Dechent, P.; Sauer, D.U. Development of a lifetime prediction model for lithium-ion batteries based on extended accelerated aging test data. *J. Power Sources* **2012**, *215*, 248–257. [[CrossRef](#)]

Disclaimer/Publisher’s Note: The statements, opinions and data contained in all publications are solely those of the individual author(s) and contributor(s) and not of MDPI and/or the editor(s). MDPI and/or the editor(s) disclaim responsibility for any injury to people or property resulting from any ideas, methods, instructions or products referred to in the content.